nature electronics

ARTICLES

https://doi.org/10.1038/s41928-020-0365-4

Raman response and transport properties of tellurium atomic chains encapsulated in nanotubes

Jing-Kai Qin[1,8], Pai-Ying Liao[1,8], Mengwei Si[1], Shiyuan Gao[2], Gang Qiu[1], Jie Jian[3], Qingxiao Wang[4], Si-Qi Zhang[5], Shouyuan Huang[6], Adam Charnas[1], Yixiu Wang[7], Moon J. Kim[4], Wenzhuo Wu[7], Xianfan Xu[6], Hai-Yan Wang[3], Li Yang[2], Yoke Khin Yap[5] and Peide D. Ye[1]*

Tellurium can form nanowires of helical atomic chains. With their unique one-dimensional van der Waals structure, these nanowires are expected to show physical and electronic properties that are remarkably different from those of bulk tellurium. Here, we show that few-chain and single-chain van der Waals tellurium nanowires can be isolated using carbon nanotube and boron nitride nanotube encapsulation. With this approach, the number of atomic chains can be controlled by the inner diameter of the nanotube. The Raman response of the structures suggests that the interaction between a single-atomic tellurium chain and a carbon nanotube is weak, and that the inter-chain interaction becomes stronger as the number of chains increases. Compared with bare tellurium nanowires on SiO_2, nanowires encapsulated in boron nitride nanotubes exhibit a dramatically enhanced current-carrying capacity, with a current density of 1.5×10^8 A cm^{-2} that exceeds that of most semiconducting nanowires. We also use our tellurium nanowires encapsulated in boron nitride nanotubes to create field-effect transistors with a diameter of only 2 nm.

Tellurium is a p-type elemental semiconductor that has recently attracted interest because of its ability to form large-area air-stable two-dimensional (2D) films with excellent transport properties[1–3]. Bulk Te has an indirect narrow bandgap of 0.35 eV with high electron and hole mobilities of ~1,000 cm^2 V^{-1} s^{-1} at room temperature[4,5]. The broken spatial inversion symmetry of the Te atomic structure gives rise to a strong spin–orbit interaction[6]. Weyl nodes have thus been predicted theoretically and observed experimentally deep in the valence band of Te[7,8]. Te also exhibits a strong response in terms of photoconductivity[9,10], piezoelectricity[11] and thermoelectricity[12,13].

Te has an anisotropic atomic structure, in which atoms are strongly bonded to two nearest neighbours, forming helical chains along the [0001] direction. These helical chains are stacked to form the Te crystal through weak van der Waals (vdW) interactions[14–16]. This unique 1D vdW crystal structure allows Te crystals to be isolated down to the single-atomic-chain limit[17–19]. Similar to layered 2D vdW materials, which usually show layer-dependent physical properties and a superior immunity to short-channel effects[20–22], this vdW-bonded 1D Te crystal composed of a single-atomic chain or few-atomic chains provides a potential scaling solution for field-effect transistor (FET) applications. The structures are also expected to exhibit intriguing physics, significantly different from the bulk form.

It is, however, difficult to study the physical properties of 1D free-standing Te atomic chains, because the atomic chains tend to be curled and their large surface area makes them very sensitive to the ambient environment. A practical route to stabilizing 1D nanowires (NWs) is to use encapsulation by carbon nanotubes (CNTs) or boron nitride nanotubes (BNNTs); this has been successfully demonstrated for a variety of organic molecules and metals[17–19,23–25]. The chemical stability of CNTs or BNNTs provides an effective chemical shielding for filling materials, and should also allow structure characterization. Previously, a single Te chain has been obtained successfully by means of single-walled carbon nanotube (SWCNT) encapsulation[17], but the chain-dependent electrical and optical properties of these NWs were not obtained. The key issue with using CNTs is that their semiconducting or metallic nature interferes with electrical measurements of the filled materials. In contrast, electrically insulating BNNTs can provide an ideal protecting layer for such materials.

In this Article, we report the synthesis of Te NWs down to a single atomic chain and the few-chain limit by filling the cavities of CNTs and BNNTs, respectively, using a physical vapour transport (PVT) technique. By controlling the inner diameter (ID) of the CNTs, few-chain and single-chain Te NWs can be isolated. We find that the frequency of Raman peaks of the samples varies monotonically with the number of Te atomic chains. Due to the excellent transport properties of Te and the high thermal conductivity of BNNTs, the current-carrying capacity of BNNT-shielded Te NWs exceeds that of most semiconductor nanowires, reaching up to 1.5×10^8 A cm^{-2}, which is only slightly smaller than the value for semiconducting SWCNTs at 4.3×10^8 A cm^{-2} (refs. [26,27]). Due to the shielding and isolation provided by the BNNTs, Te NWs at the few-chain limit could stably exist in ambient, and the short-channel Te NW FETs exhibit decent electrical performance, even with a diameter of only 2 nm.

[1]School of Electrical and Computer Engineering, Purdue University, West Lafayette, IN, USA. [2]Department of Physics and Institute of Materials Science and Engineering, Washington University in St Louis, St Louis, MO, USA. [3]School of Materials Science and Engineering, Purdue University, West Lafayette, IN, USA. [4]Department of Materials Science and Engineering, University of Texas at Dallas, Richardson, TX, USA. [5]Department of Physics, Michigan Technological University, Houghton, MI, USA. [6]School of Mechanical Engineering, Purdue University, West Lafayette, IN, USA. [7]School of Industrial Engineering, Purdue University, West Lafayette, IN, USA. [8]These authors contributed equally: Jing-Kai Qin, Pai-Ying Liao. *e-mail: yep@purdue.edu

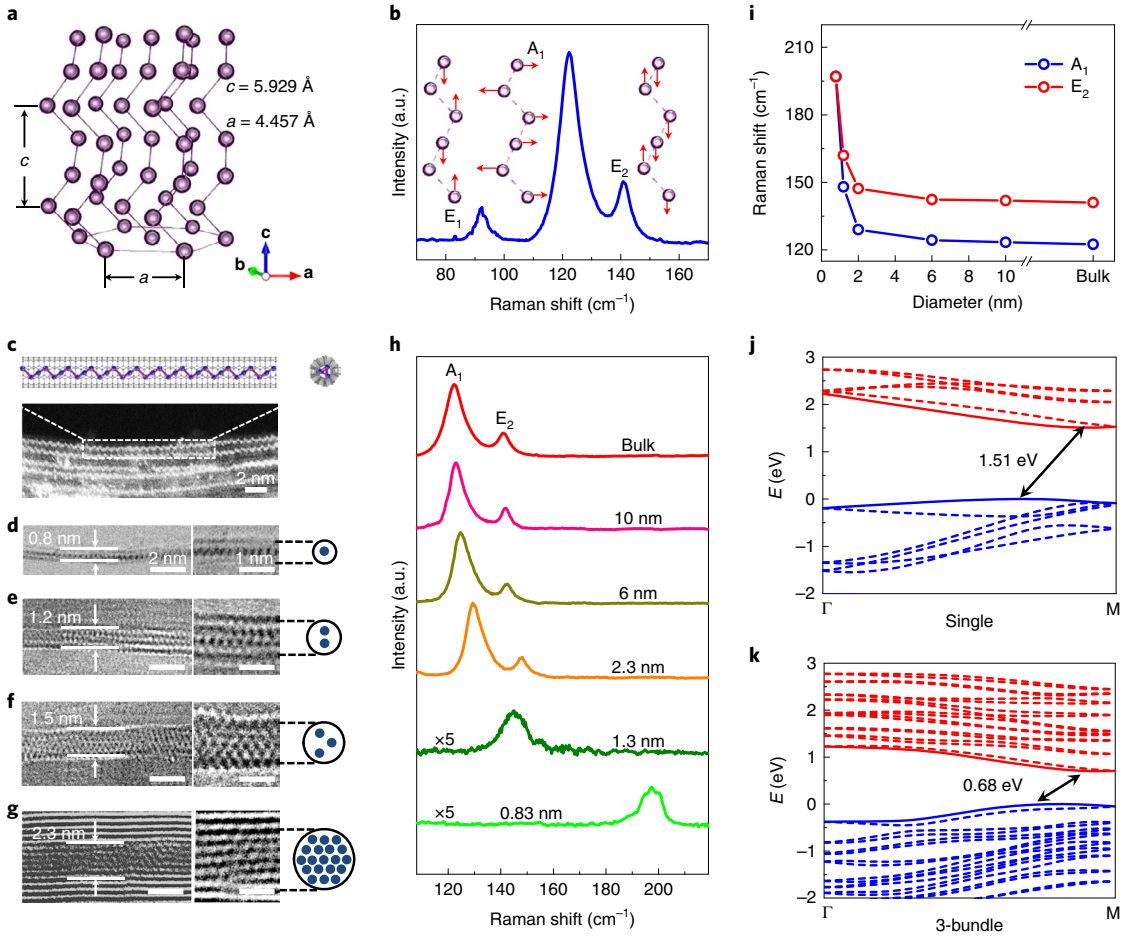

Fig. 1 | Characterization of Te NWs isolated down to the few-chain limit by CNT encapsulation. a, Atomic structure of hexagonal Te. **b**, Raman spectrum obtained in bulk Te crystal. Inset: images showing the displacement pattern for vibration modes E_1, A_1 and E_2. **c**, HAADF-STEM image of a single Te chain in a 0.8 nm SWCNT, where helical coils with clear three-fold symmetry are distinguished. Inset: corresponding schematic illustration. **d**–**g**, HRTEM images of the single (**d**), double (**e**), triple (**f**) and 19 (**g**) chains of Te shielded by CNTs. Insets: schematic structure diagrams. **h**, Raman spectrum evolution of Te NWs with CNTs of different ID. **i**, Dependence of the shifts in Raman peak frequency on CNT ID. **j**, Band structure of a single Te atomic chain. **k**, Band structure of triple Te atomic chains.

Raman response of single-chain Te NWs in CNTs

Figure 1a shows the atomic structure of the trigonal Te lattice. Each atom is covalently bonded periodically with its two nearest neighbours along the *c* axis to form into a helical chain, yielding an equilateral triangle projection on the basal plane. Arrays of parallel chains are stacked together by weak vdW forces and arranged hexagonally. A variety of CNTs with different IDs were taken as templates (Supplementary Fig. 1), and in a given batch more than 90% of the SWCNTs were successfully filled with Te atomic chains (Supplementary Fig. 2). High-angle annular dark-field scanning transmission electron microscopy (HAADF-STEM) and high-resolution TEM (HRTEM) images demonstrated that a single Te atomic chain can exist in ambient with a 0.8 nm SWCNT as a container, and the individual Te atoms can be distinctively resolved with a clear three-fold-symmetry helical structure (Fig. 1c,d). The successful realization of a single atomic chain is ascribed to the unique 1D vdW nature of Te. Given that a single Te atom tends to bond covalently only with its two neighbouring atoms in a chain, a single atomic chain of Te can be isolated by spatial confinement using a SWCNT. Using SWCNTs with IDs of 1.2 and 1.5 nm increases the number of confined Te atomic chains to 2 and 3, respectively, and a larger-diameter multiwalled CNT (MWCNT) of 2.3 nm results in a wider Te NW with ~19 Te atomic chains (Fig. 1e–g and Supplementary Fig. 3). The results suggest that, by carefully selecting the CNT ID, controlled growth of ultranarrow Te NWs with few atomic chains can be realized.

Raman spectroscopy, a powerful non-destructive characterization tool, has been widely used to investigate material properties and layer-to-layer interactions (here chain-to-chain) via lattice vibrations[28]. Consistent with theoretical analysis[15,16], three first-order Raman active modes, E_1, A_1 and E_2, located at 92 cm^{-1}, 123 cm^{-1} and 140 cm^{-1}, respectively, can be clearly detected in bulk trigonal Te (Fig. 1b). The insets in Fig. 1b illustrate the vibration pattern of the Raman modes. The A_1 mode is caused by chain expansion, where each atom moves in the basal plane, whereas the E_1 and E_2 modes represent bond-bending and bond-stretching with a larger admixture, respectively[16]. In 2D materials, the Raman frequency is very sensitive to the number of layers, because the vdW interaction can strongly affect electron–phonon coupling, resulting in changed phonon modes[28]. The Raman technique can also therefore be used to evaluate the vdW interaction in a Te NW crystal and identify the number of atomic chains. For a single Te atomic chain confined in a 0.8 nm SWCNT, the A_1 mode exhibits a large shift towards higher frequency at 196 cm^{-1}, while the E_1 and E_2 modes are too weak to be detected (Supplementary Fig. 5). This result is in good agreement with our theoretical calculations for the

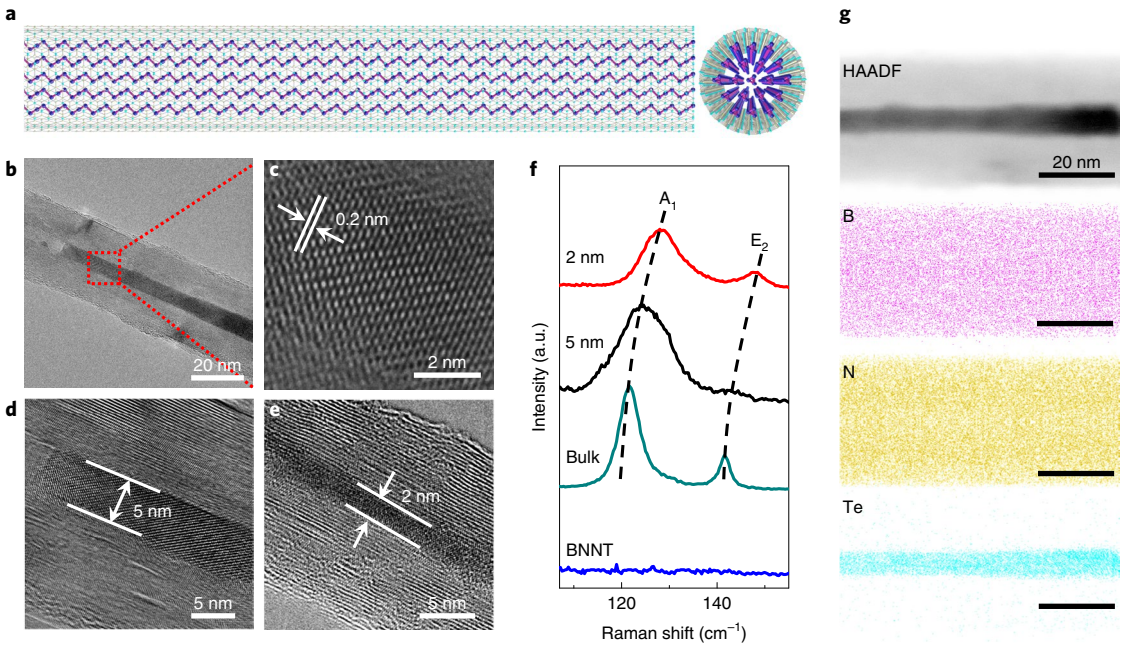

Fig. 2 | Characterization of few-chain Te NWs shielded by BNNTs. a, Schematic of a Te-BNNT. **b**, TEM image of a 5 nm Te NW in a BNNT. **c**, Enlarged HRTEM image of the region outlined in red in **b**. **d**,**e**, HRTEM images of BNNTs filled with 5 nm (**d**) and 2 nm (**e**) Te NWs. **f**, Raman spectrum comparison of Te NWs in BNNTs with different diameters as indicated. **g**, HAADF-STEM image and EDS maps showing the chemical composition of the filling material.

free-standing single Te chain (Supplementary Figs. 6 and 7). This suggests that the vdW interaction between the single Te atomic chain and the SWCNT inner wall is very weak and the Te chain could be fully relaxed in the SWCNT and exist stably in the form of a three-fold-symmetry helical coil, as shown in Fig. 1c. Figure 1h,i presents the evolution of Raman peak frequency with Te NW diameter. As the number of Te atomic chains increases from 2 towards bulk (the ID of the CNT increases from 1.3 nm to >10 nm), clear redshifts of the A_1 and E_2 modes can be observed. For example, the A_1 peak is significantly shifted from 148 cm^{-1} for 1.3 nm to 123.1 cm^{-1} for bulk (Supplementary Fig. 4). Similar to the previously reported results for few-layer Te[1], the unique chiral structure of Te causes weakening of intra-chain covalent atomic bonding and enhancement of inter-chain vdW interactions as the number of layers increases. Therefore, Te atoms can more easily restore back into the bulk form, resulting in Raman frequency reduction of the A_1 vibration mode. By contrast, long-range Coulomb interactions dominate the vibration mode of individual Te atomic chains in few-chain samples and lead to hardening of the intra-chain E vibration modes[29]. A greater number of Te chains would split the E_1 mode, thus introducing too much inaccuracy for the definition of peak positions; accordingly, we only focus on the A_1 and E_2 modes in this study.

Density functional theory (DFT) calculations revealed that the electronic structure of Te NWs is highly dependent on the number of chains. According to a previous study[30], lone-pair and anti-bonding orbitals lead to an indirect bandgap of 0.35 eV in bulk Te. As the number of chains decreases, the indirect bandgap becomes more prominent. As shown in Fig. 1j,k, the bandgap is expected to increase monotonically to 0.68 eV for three Te chains, and eventually reach 1.51 eV in the single-chain limit due to the quantum confinement effect[31]. Our theoretical results also show that adjacent chains in Te are indeed strongly coupled with each other, with a high cleavage energy of 400 meV per atom, far exceeding that of graphene (60 meV per atom). This explains the difficulty in isolating a single atomic chain of Te using a conventional exfoliation technique.

Although few-chain Te NWs could be protected well from ambient degradation by CNT encapsulation, the dominant electrical conductivity of CNTs prevents direct electrical measurements of the shielded Te NWs. BNNTs are electrically insulating, with the same hollow structure as CNTs, and are also promising 1D nanoscale containers for guest species such as metals, metal halides and molecules[24,32,33]. Here, we demonstrate that BNNTs grown by chemical vapour deposition (CVD) are an ideal template to encapsulate few-chain Te NWs using the same PVT technique as used with CNTs (Supplementary Figs. 8 and 9). Because BNNTs are electrically insulating, it is possible to perform direct electrical measurements on Te NWs down to the few-chain limit[34,35].

Raman response of few-chain Te NWs in BNNTs

Figure 2a presents a schematic of an ultranarrow Te NW shielded by a BNNT (Te-BNNT). Before filling, the caps of the nanotubes were first removed by ammonium hydroxide etching (see Methods). Figure 2b shows a representative TEM image of an individual Te NW inside a BNNT; the Te-filled section exhibits a clearly different contrast in the BNNT cavity. Combined with the X-ray energy dispersive spectroscopy (EDS) elemental mapping shown in Fig. 2g, we confirmed that elemental Te NWs can be successfully confined inside the cavity of a BNNT. HRTEM images show that Te NWs confined in BNNTs crystallize homogeneously in the form of a single crystal; distinctive lattice fringes belonging to the Te NW can be observed clearly, suggesting that the Te NW is well crystallized with high quality (Fig. 2c and Supplementary Fig. 10). Note that the filling length of Te NWs in BNNTs is usually less than 400 nm, which is much shorter than in CNTs. This is attributed to the polarity of the interatomic B–N bonding and delocalization of π electrons in BNNTs, which lead to strong interface interactions between the inner BNNT surface and the filled Te atoms, restricting high-aspect-ratio filling[24]. In our experiments, the narrowest diameter of Te NW achieved was 2 nm, corresponding to ~19 individual Te atomic chains inside a BNNT cavity (Fig. 2d,e). As was previously done for CNTs, Raman frequency shifts were used to determine the diameters of Te NWs encapsulated by the BNNTs. The A_1 mode of a Te-BNNT with 5 nm ID exhibits a blueshift of 2.4 cm^{-1} compared with the bulk form (~121.2 cm^{-1}), and the vibration fre-

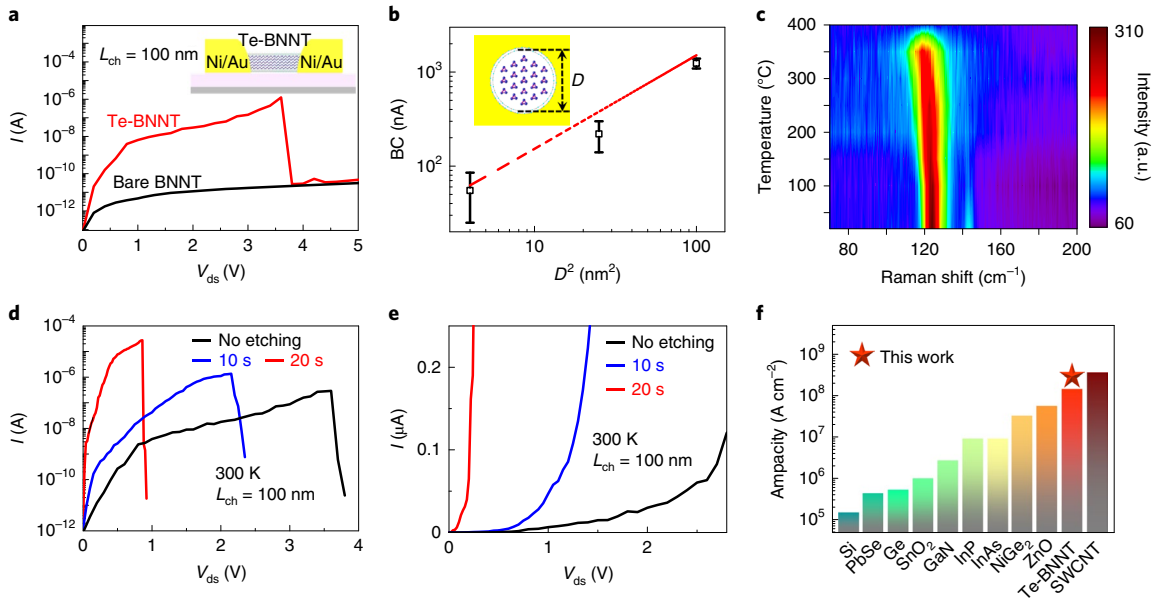

Fig. 3 | Current-carrying capability of Te NWs encapsulated in BNNTs. a, *I*–*V* curves up to breakdown of a Te-BNNT device with 100 nm channel length and an empty (bare) BNNT device. **b**, Breakdown current (BC) versus D^2 with channel lengths of 100 nm. **c**, Mapping plot of in situ temperature-dependent Raman spectra of a Te-BNNT. **d**,**e**, Logarithmic-scale (**d**) and linear-scale (**e**) plots of the *I*–*V* characteristics of Te-BNNT devices with different etching times. **f**, Comparison of the ampacity of Te-BNNTs and other semiconductor NWs.

quency continues to shift up to 129.2 cm^{-1} as the diameter of the Te NW is reduced to 2 nm (Fig. 2f and Supplementary Fig. 11). We thus applied Raman spectroscopy to determine the diameter of Te NWs in BNNTs and located the samples for device fabrication after being transferred onto a SiO_2/Si substrate.

Current-carrying capacity of few-chain Te-BNNT devices

To investigate the electrical properties of few-chain Te NWs, we first fabricated two-terminal devices with an isolated Te-BNNT as the channel material on a Si substrate, with 90 nm SiO_2 as the gate dielectric. Ni/Au (30/100 nm) electrodes were patterned using electron-beam lithography followed by electron-beam evaporation of metals and a liftoff process. Short-channel (100 nm) devices were fabricated to ensure the channel region was fully filled by the Te NW. Empty BNNT devices were also tested for comparison. As the *I*–*V* characteristics in Fig. 3a show, the current of a Te-BNNT device with a diameter of 10 nm has about four orders of magnitude higher current-carrying capacity than the empty BNNT device with the same configuration, which confirms that the Te NW is responsible for the channel conduction and not the BNNT. The device could sustain a large V_{ds}, and the current does not show any saturation until device breakdown at $V_{max} = 3.6$ V and $I_{max} = 1.2$ μA. The diameter-dependent breakdown current of ultranarrow Te NWs was also measured based on devices with 100 nm channel lengths. Although the encapsulated Te NWs have varying diameters, BNNTs with different diameters usually have a similar thickness (>10 nm), as observed in HRTEM images, so the breakdown current is mainly determined by the intrinsic properties of the inner Te NWs. For devices with a D^2 (inset of Fig. 3b) of 100 nm^2, the average breakdown current was determined to be ~1.2 μA. Reduction of D^2 leads to a scaling down of the current-carrying capacity of Te, and the smallest average current measured was 62 nA for devices filled with 2 nm Te NWs. The values of ampacity in different devices are fitted linearly with D^2 in Fig. 3b. The realization of electrical measurements of few-chain Te NWs is enabled by the efficient dissipation of Joule heating by the BNNT encapsulation[36]. In situ temperature-dependent Raman spectroscopy was conducted to explore the temperature limit of this passivation, and the corresponding mapping plot is presented in Fig. 3c. Te NWs shielded by BNNTs sustained high temperatures up to 350 °C, whereas the naked NWs prepared by a solution process were easily damaged at 250 °C (Supplementary Figs. 12 and 16). The Raman peaks of Te tend to shift towards low frequency as the temperature increases; this is related to a non-crystallized phase change induced by high temperature[37].

The BN encapsulation protects the few-chain Te NWs from damage during measurements, but it also introduces a large electrical contact resistance, resulting in reduced channel current. Taking this into consideration, an accurate and selective BN etching process was developed to directly control the thinning of the BNNT insulator layer. Figure 3d,e shows the *I*–*V* curves of typical devices as a function of etching time. Notably, the breakdown current is greatly enhanced up to 29 μA after 20 s of etching, almost 100 times larger than in the un-etched reference devices. The total resistance of the device after 20 s of etching is calculated to be 1.6 kΩ μm, which is one order of magnitude smaller than that of devices without etching (~21 kΩ μm). It is worth noting that over-etching the BN layer deteriorates the performance of Te-BNNT devices (Supplementary Fig. 17). This result can be ascribed to a high Schottky barrier at the Ni/Te contact interface. The value of current capacity for the Te-BNNT devices reaches up to 1.5×10^8 A cm^{-2}, almost two orders of magnitude larger than in bare Te NW devices (7.4×10^6 A cm^{-2}; Supplementary Fig. 14). This value exceeds those for most reported semiconductor NWs[38–45] (Fig. 3f and Supplementary Table 1), and it is also higher than those from the high-ampacity $TaSe_3$ and $ZrTe_3$ quasi-1D metallic nanowires[46,47]. Indeed, it is only slightly smaller than semiconducting SWCNTs with a similar configuration (~3.0–8.8×10^8 A cm^{-2})[26,27]. Such dramatic enhancement of ampacity can be attributed to the high mobility of Te NWs, the extremely high thermal conductivity of BN (~360 W m^{-1} K^{-1}) and the low electrical and thermal resistance at the BN/Te interface[48]. The excellent current-carrying capacity of Te-BNNT strongly suggests that this nanomaterial system has potential for future electronics applications, especially high-performance FETs with ultrashort channels.

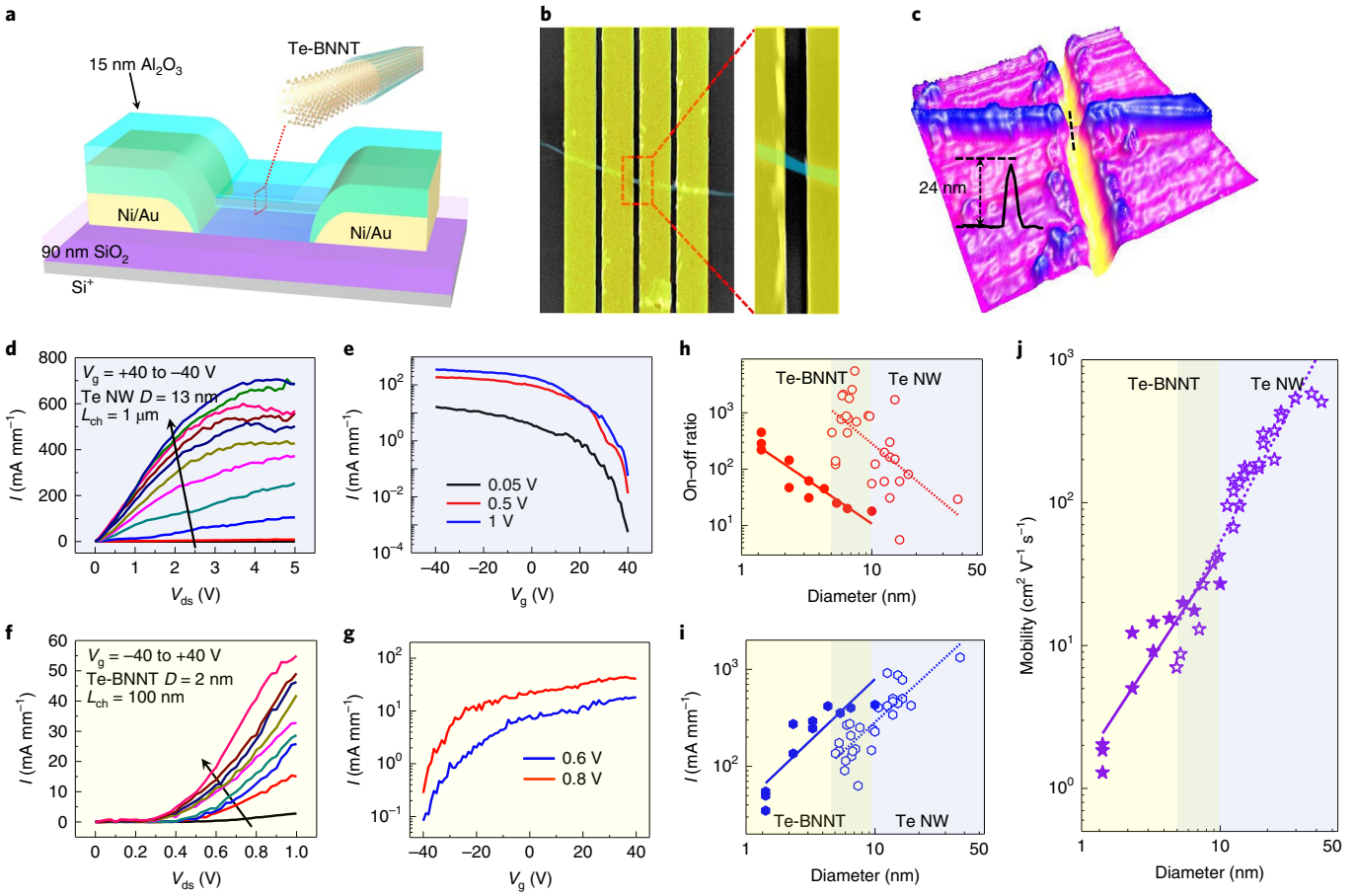

Fig. 4 | Electrical measurements of transistors based on few-chain Te NWs. a, Schematic of an individual Te-BNNT FET. **b**,**c**, False-coloured SEM image (**b**) and AFM height profile (**c**) of a representative FET device before Al_2O_3 capping. **d**, Output characteristics of a typical p-type Te NW transistor with a diameter of ~13 nm. **e**, Corresponding transfer curves of the same device. **f**, Output characteristics of an n-type Te-BNNT transistor with a diameter of ~2 nm after 15 nm Al_2O_3 film capping. **g**, Corresponding transfer curve, exhibiting typical n-type transport behaviour with an on/off ratio of 450 at V_{ds} = 0.6 V. **h**–**j**, On/off ratio (**h**), current density at V_{ds} = 1 V (**i**) and carrier mobility (**j**) of Te-BNNTs and Te NWs short-channel FETs. Filled symbols represent Te-BNNT NW devices and open symbols represent bare Te NW devices.

Transport properties of Te-BNNT FETs

The electrical characteristics of FETs based on Te NWs were also systematically studied. Note that the diameters of ultranarrow Te NWs shielded by BNNTs are restricted to less than 10 nm due to the ID limitation of BNNTs, whereas Te NWs with larger diameters can be obtained effectively using a substrate-free solution process (for details see Methods). Thus, two types of Te NW were systematically investigated: ultranarrow Te NWs in BNNTs with diameters of 2–10 nm and solution-grown Te NWs with diameters of 6–40 nm. Figure 4a presents a typical schematic of a FET device based on a Te-BNNT, in which an Al_2O_3 capping layer grown by low-temperature atomic-layer deposition can dope the channel and change the FET characteristics from p-type to n-type. Figure 4b shows a false-coloured scanning electron microscopy (SEM) image of some short-channel devices, where the outer diameter of the Te-BNNT was measured to be 24 nm by atomic force microscopy (AFM) (Fig. 4c). Figure 4d,e presents the electrical performance of a Te NW FET with a diameter of 13 nm measured at room temperature. The device exhibits typical p-type characteristics with an on/off ratio on the order of ~1×10^4 at a small V_{ds} of 0.05 V, with an on-state drain current of up to 700 mA mm^{-1} at V_g = −40 V, normalized by the diameter. Short-channel (100 nm) devices were also fabricated for comparison (Supplementary Fig. 13). The diameter dependence of the on/off ratio and maximum drain current based on long-channel devices was also systematically studied, with data taken from more than 30 devices (Supplementary Fig. 15). Due to the enhanced gate electrostatic control in narrow NWs, the on/off ratio increases sharply from ~1×10^2 to ~1×10^5 as the diameter decreases from 40 to 6 nm. However, the current density exhibits the opposite trend in narrower samples because they are more susceptible to surface oxidization and defects. Indeed, FETs on ultranarrow bare Te NWs less than 6 nm in diameter start to lose electrical conductance and gate control, because the crystalline structure of Te at this scale cannot be well preserved in ambient for a long time during device fabrication and measurement.

For Te-BNNT devices with typical metal–semiconductor (MS) or metal–insulator–semiconductor (MIS) contacts, the current of the channel is mainly limited by the contact resistance, which is determined by two factors: the Schottky barrier height/width and the tunnelling resistance of the inserted ultrathin insulator[49]. Although Ni has a relatively high work function that is close to the Fermi level of unintentionally p-doped bulk Te, direct contact at an MS interface results in a high Schottky barrier height for ultranarrow Te NWs due to an enhanced bandgap (a result of the quantum confinement effect; Fig. 1j,k)[50]. A large Schottky barrier height leads to a large contact resistance at the Ni/Te contact. Few-layer BNNT in the contact region, after selective dry etching, could provide a perfect insulating layer for the inner Te NW (avoiding process

damage); the thickness of the BN layer thus needs to be optimized to realize the maximum current-carrying capacity in devices. The shielding of the BNNT enables Te-BNNT devices to be electrically functionalized with Te NWs with diameters as small as 2 nm (Supplementary Fig. 18). More interestingly, the transport characteristics of Te-BNNT FETs show n-type behaviour after Al_2O_3 capping, indicating that the classical Fermi-level pinning issue does not exist in Te-BNNTs[51]. The 2 nm device possesses a large on-state current of up to 50 mA mm^{-1} at $V_{ds} = 1$ V (Fig. 4f). Such a high current is comparable to that in monolayer MoS_2 transistors with the same short-channel length ($I_{max} = 42$ mA mm^{-1}, $V_{ds} = 0.8$ V, $L_{ch} = 100$ nm)[52]. Note that the output curves showing non-ideal characteristics at low V_{ds} are due to the insulating BN layer sandwiched at the Ni/Te interface. Figure 4g presents the transfer characteristics of the same device at $V_{ds} = 0.6$ V and 0.8 V and shows a decent on/off current ratio (>10^2), comparable to that of black phosphorus transistors with 100 nm channel length[53]. Low-temperature atomic-layer-deposited Al_2O_3 has a large number of positive fixed charges in the dielectric and can be used as an n-type dielectric doping layer for a p-type 2D Te film[5,54]. The situation here is even more interesting: the Al_2O_3 capping layer serves as a low-work-function material that lifts up the Fermi level in the Te NW and makes it an n-type FET. The large drain current obtained on the n-type Te-BNNT FET reflects the fact that the electron mobility of Te is as high as the hole mobility in Te[5].

Figure 4h,i shows that encapsulated Te-BNNT devices continue to demonstrate electrical performance with Te NWs down to 2 nm diameter, while in bare Te NW devices the diameter is limited to 6 nm. As summarized in Fig. 4j, Te NWs exhibit excellent carrier mobility, larger than ~600 cm^2 V^{-1} s^{-1} for a diameter of 25 nm. The reduction of mobility in narrower samples can be ascribed to surface oxidation and defects, with a significant increase in surface-to-volume ratio. The carrier mobility decreases with smaller-diameter Te NWs and the average carrier mobility for the smallest 2 nm Te NW is ~1.85 cm^2 V^{-1} s^{-1} (Supplementary Fig. 19).

Conclusions

We have reported the isolation of 1D vdW Te NWs at the few-chain and single-chain limit using CNTs as a growth template. The lattice vibrations of the structures exhibit a clear dependence on the number of Te atomic chains, which can be observed as peak shifts in the Raman frequency. By encapsulation within BNNTs, we were able to measure the electrical transport properties for few-chain Te NWs (down to ~19 atomic chains), and both p-type and n-type Te FETs with few atomic chains as channels were demonstrated. The current-carrying ability of semiconducting Te NWs exceeds the values measured in conventional semiconductor NWs after BNNT encapsulation and contact engineering.

Methods

Encapsulating Te NWs in CNTs and BNNTs. A variety of CNTs with different IDs were purchased from Sigma-Aldrich. Detailed characterizations of the CNTs are provided in the Supplementary Information. Before filling, 26 mg of CNTs were heated at 420 °C for 1 h in ambient to open the ends of tubes. BNNTs were obtained by a growth vapour trapping (GVT) approach (for details see Supplementary Information). The caps of the BNNTs were removed by ultrasonicating in 10% ammonium hydroxide solution for 4 h, followed by thermal treatment at 800 °C in air for 1 h. Cap-opened CNTs/BNNTs and 70 mg of Te (Sigma-Aldrich, 99.8% trace metals) were sealed under vacuum (10^{-5} mbar) in a quartz tube and heated at 439 °C for four days. As-prepared Te-CNTs or Te-BNNTs were dispersed ultrasonically into methanol for subsequent characterization.

Preparation of Te NWs by a substrate-free solution process. Analytical-grade Na_2TeO_3 (0.0015 mol, Sigma-Aldrich, 99.9% trace metals) and polyvinylpyrrolidone (1 g, Sigma-Aldrich, 99.9% trace metals) were dissolved in distilled water (100 ml) to form a homogeneous solution, which was sealed into a Teflon-lined stainless-steel autoclave together with an aqueous ammonia solution (25%, wt/wt%) and hydrazine hydrate (80%, wt/wt%). The reaction was conducted at 180 °C for 3 h, and then cooled to room temperature naturally. Finally, the products were precipitated by centrifugation at 5,000 r.p.m. for 5 min and washed with distilled water to remove residuals.

HRTEM and Raman characterization. A dispersion of Te-CNTs or Te-BNNTs was drop cast onto a Si substrate with 90 nm SiO_2 as gate dielectric for Raman analysis. To eliminate the influence of CNT radial breathing modes (ranging from 150 cm^{-1} to 180 cm^{-1}), AFM was used to locate the testing area where CNTs were sparsely distributed on the substrate[55]. Raman measurements were performed using a HORIBA LabRAM HR800 Raman spectrometer. This system was equipped with a He–Ne excitation laser (633 nm wavelength). Before measurements, the system was calibrated with the Raman peak of Si at 521 cm^{-1}. In situ temperature-dependent Raman spectroscopy was conducted by heating samples on a hot plate from room temperature to 400 °C in steps of 50 °C. Spectra were only collected after the temperature remained stable for 5 min in ambient. For TEM characterization, a powder sample of CNTs was first dissolved in methanol, followed by 10 min of ultrasonic treatment. Three drops of the solution were then dropped onto a 3 mm TEM grid supported by lacey carbon film. HRTEM was performed with a FEI Talos F200x system equipped with a probe corrector. This microscope was operated with an acceleration voltage of 200 kV. STEM imaging was carried out using a JEM-ARM200F microscope equipped with a CEOS probe aberration corrector. To reduce beam damage of the CNTs and encapsulated Te, the microscope was operated at 80 kV. The convergence semi-angle and the current of the electron probe were 25 mrad and 23 pA, respectively. HAADF imaging was performed using a JEOL dark-field detector, with the collection semi-angle ranging from 40 to 150 mrad.

Device fabrication and electrical measurements. After determining the diameter of Te NWs encapsulated in BNNT by Raman spectroscopy, source/drain regions were patterned by electron-beam lithography, followed by electron-beam evaporation of 30 nm Ni and 100 nm Au as metal contacts. The devices were measured with a probe station connected to a semiconductor characterization system (4200SCS, Keithley) at room temperature. For thinning of BN at the contact areas, Ar/SF_6 plasma with power of 75 W and pressure of 50 Pa was used with different irradiation times at room temperature.

DFT calculations. The band structure and phonon energy were obtained from DFT calculations using the Quantum ESPRESSO package. The norm-conserving pseudopotential within the generalized gradient approximation of Perdew–Burke–Ernzerhof (GGA-PBE) was used. The plane-wave basis was set to an energy cutoff of 60 Ry. The k-point sampling of the Brillouin zone was $1 \times 1 \times 12$ for the single chain and three-chain bundle, and $8 \times 8 \times 6$ for bulk Te. The structure was relaxed until the total energy converged to within 1×10^{-6} Ry. The 1D chains were separated with a vacuum region over 15 Å with its periodic images. The band structures were calculated including the spin–orbit interaction.

Data availability

The data that support the plots within this paper and other findings of this study are available from the corresponding author upon reasonable request.

Received: 29 May 2019; Accepted: 6 January 2020;
Published online: 10 February 2020

References

1. Wang, Y. et al. Field-effect transistors made from solution-grown two-dimensional tellurene. *Nat. Electron.* **1**, 228–236 (2018).
2. Qiu, G. et al. Quantum transport and band structure evolution under high magnetic field in few-layer tellurene. *Nano Lett.* **18**, 5760–5767 (2018).
3. Zhu, Z. et al. Multivalency-driven formation of Te-based monolayer materials: a combined first-principles and experimental study. *Phys. Rev. Lett.* **119**, 106101 (2017).
4. Peng, H., Kioussis, N. & Snyder, G. J. Elemental tellurium as a chiral p-type thermoelectric material. *Phys. Rev. B* **89**, 195206 (2016).
5. Qiu, G. et al. High-performance few-layer tellurium CMOS devices enabled by atomic layer deposited dielectric doping technique. In *Proceedings of the 76th Device Research Conference* (IEEE, 2018).
6. Agapito, L., Kioussis, N., Goddard, W. A. III & Ong, N. P. Novel family of chiral-based topological insulators: elemental tellurium under strain. *Phys. Rev. Lett.* **110**, 176401 (2013).
7. Hirayama, M., Okugawa, R., Ishibashi, S., Murakami, S. & Miyake, T. Weyl node and spin texture in trigonal tellurium and selenium. *Phys. Rev. Lett.* **114**, 206401 (2015).
8. Nakayama, K. et al. Band splitting and Weyl nodes in trigonal tellurium studied by angle-resolved photoemission spectroscopy and density functional theory. *Phys. Rev. B* **95**, 125204 (2017).
9. Wang, Q. S. et al. Van der Waals epitaxy and photoresponse of hexagonal tellurium nanoplates on flexible mica sheets. *ACS Nano* **8**, 7497–7505 (2014).
10. Amani, M. et al. Solution-synthesized high-mobility tellurium nanoflakes for short-wave infrared photodetectors. *ACS Nano* **12**, 7253–7263 (2018).

11. Lee, T. et al. High-power density piezoelectric energy harvesting using radially strained ultrathin trigonal tellurium nanowire assembly. *Adv. Mater.* **25**, 2920–2925 (2013).
12. Lin, S. Q. et al. Tellurium as a high-performance elemental thermoelectric. *Nat. Commun.* **7**, 10287 (2016).
13. Qiu, G. et al. Thermoelectric performance of 2D tellurium with accumulation contacts. *Nano Lett.* **19**, 1955–1962 (2019).
14. Doi, T., Nakao, K. & Kamimura, H. The valence band structure of tellurium. I. The *k·p* perturbation method. *J. Phys. Soc. Jpn* **28**, 36–43 (1970).
15. Martin, R. M., Lucovsky, G. & Helliwell, K. Intermolecular bonding and lattice dynamics of Se and Te. *Phys. Rev. B* **13**, 1383–1395 (1976).
16. Du, Y. C. et al. One-dimensional van der Waals material tellurium: Raman spectroscopy under strain and magneto-transport. *Nano Lett.* **17**, 3965–3973 (2017).
17. Medeiros, P. V. C., Marks, S., Wynn, J. M. & Vasylenko, A. Single-atom scale structural selectivity in Te nanowires encapsulated inside ultranarrow, single-walled carbon nanotubes. *ACS Nano* **11**, 6178–6185 (2017).
18. Pham, T. et al. Torsional instability in the single-chain limit of a transition metal trichalcogenide. *Science* **361**, 263–266 (2018).
19. Kobayashi, K. & Yasuda, H. Structural transition of tellurium encapsulated in confined one-dimensional nanospaces depending on the diameter. *Chem. Phys. Lett.* **634**, 60–65 (2015).
20. Li, H. et al. From bulk to monolayer MoS_2: evolution of Raman scattering. *Adv. Funct. Mater.* **22**, 1385–1390 (2012).
21. Desai, S. B. et al. MoS_2 transistors with 1-nanometer gate lengths. *Science* **354**, 99–102 (2016).
22. Javey, A. et al. High-field quasiballistic transport in short carbon nanotubes. *Phys. Rev. Lett.* **92**, 106804 (2004).
23. Komsa, H.-P., Senga, R., Suenaga, K. & Krasheninnikov, A. V. Structural distortions and charge density waves in iodine chains encapsulated inside carbon nanotubes. *Nano Lett.* **17**, 3694–3700 (2017).
24. Walker, K. E. et al. Growth of carbon nanotubes inside boron nitride nanotubes by coalescence of fullerenes: toward the world's smallest coaxial cable. *Small Methods* **1**, 1700184 (2017).
25. Nieto-Ortega, B. et al. Band-gap opening in metallic single-walled carbon nanotubes by encapsulation of an organic salt. *Angew. Chem. Int. Ed.* **56**, 12240–12244 (2017).
26. Franklin, A. D. & Chen, Z. Length scaling of carbon nanotube transistors. *Nat. Nanotechnol.* **5**, 858–862 (2010).
27. Seidel, R. V. et al. Bias dependence and electrical breakdown of small diameter single-walled carbon nanotubes. *J. Appl. Phys.* **96**, 6694–6699 (2004).
28. Plechinger, G. et al. Scanning Raman spectroscopy of few- and single-layer MoS_2 flakes. *Proc. SPIE* **8463**, 84630N (2012).
29. Wang, X. et al. Highly anisotropic and robust excitons in monolayer black phosphorus. *Nat. Nanotechnol.* **10**, 517–521 (2015).
30. Coker, A., Lee, T. & Das, T. P. Investigation of the electronic properties of tellurium-energy-band structure. *Phys. Rev. B* **22**, 2968–2975 (1980).
31. Andharia, E. et al. Exfoliation energy, quasiparticle band structure, and excitonic properties of selenium and tellurium atomic chains. *Phys. Rev. B* **98**, 035420 (2018).
32. Pham, T. et al. A universal wet-chemistry route to metal filling of boron nitride nanotubes. *Nano Lett.* **16**, 320–325 (2016).
33. Nautiyal, P., Gupta, A., Seal, S., Boesl, B. & Agarwal, A. Reactive wetting and filling of boron nitride nanotubes by molten aluminum during equilibrium solidification. *Acta Mater.* **126**, 124–131 (2017).
34. Lee, C. H., Xie, M., Kayastha, V., Wang, J. & Yap, Y. K. Patterned growth of boron nitride nanotubes by catalytic chemical vapor deposition. *Chem. Mater.* **22**, 1782–1787 (2010).
35. Lee., C. H. et al. Room-temperature tunneling behavior of boron nitride nanotubes functionalized with gold quantum dots. *Adv. Mater.* **25**, 4544–4548 (2013).
36. Huang, J. W. et al. Superior current carrying capacity of boron nitride encapsulated carbon nanotubes with zero-dimensional contacts. *Nano Lett.* **15**, 6836–6840 (2015).
37. Pine, A. S. & Dresselhaus, G. Raman spectra and lattice dynamics of tellurium. *Phys. Rev. B* **4**, 356–371 (1971).
38. Wurz, J., Logeeswaran, V. J., Sarkar, A. & Saif Islam, M. High current density and failure mechanism in epitaxially bridged silicon nanowires. In *Proceedings of 8th IEEE Conference on Nanotechnology* (IEEE, 2008).
39. Liang, W. et al. Field-effect modulation of Seebeck coefficient in single PbSe nanowires. *Nano Lett.* **9**, 1689–1693 (2009).
40. Tang, J. et al. Single-crystalline $Ni_2Ge/Ge/Ni_2Ge$ nanowire heterostructure transistors. *Nanotechnology* **21**, 505704 (2010).
41. Nie, A., Liu, J., Dong, C. & Wang, H. Electrical failure behaviors of semiconductor oxide nanowires. *Nanotechnology* **22**, 405703 (2011).
42. Westover, T. et al. Photoluminescence, thermal transport, and breakdown in Joule-heated GaN nanowires. *Nano Lett.* **9**, 257–263 (2008).
43. Wallentin, J. et al. Probing the wurtzite conduction band structure using state filling in highly doped InP nanowires. *Nano Lett.* **11**, 2286–2290 (2011).
44. Dayeh, S. A., Susac, D., Kavanagh, K. L., Yu, E. T. & Wang, D. Field dependent transport properties in InAs nanowire field effect transistors. *Nano Lett.* **8**, 3114–3119 (2008).
45. Hu, Y. et al. Observation of a 2D electron gas and the tuning of the electrical conductance of ZnO nanowires by controllable surface band bending. *Adv. Funct. Mater.* **19**, 2380–2387 (2009).
46. Stolyarov, M. A. et al. Breakdown current density in h-BN-capped quasi-1D $TaSe_3$ metallic nanowires: prospects of interconnect applications. *Nanoscale* **8**, 15774–15782 (2016).
47. Geremew, A. et al. Current carrying capacity of quasi-1D $ZrTe_3$ van der Waals nanoribbons. *IEEE Electron Device Lett.* **39**, 735–738 (2018).
48. Jo, I. et al. Thermal conductivity and phonon transport in suspended few-layer hexagonal boron nitride. *Nano Lett.* **13**, 550–554 (2013).
49. Wang, J. et al. High mobility MoS_2 transistor with low Schottky barrier contact by using atomic thick *h*-BN as a tunneling layer. *Adv. Mater.* **28**, 8302–8308 (2016).
50. Pan, Y., Gao, S., Yang, L. & Lu, J. Dependence of excited-state properties of tellurium on dimensionality: from bulk to two dimensions to one dimension. *Phys. Rev. B* **98**, 085135 (2018).
51. Léonard, F. & Tersoff, J. Role of Fermi-level pinning in nanotube Schottky diodes. *Phys. Rev. Lett.* **84**, 4693 (2000).
52. Liu, H., Neal, A. T. & Ye, P. D. Channel length scaling of MoS_2 MOSFETs. *ACS Nano* **6**, 8563–8569 (2012).
53. Miao, J., Zhang, S., Cai, L., Scherr, M. & Wang, C. Ultrashort channel length black phosphorus field-effect transistors. *ACS Nano* **9**, 9236–9243 (2015).
54. Berweger, S. et al. Imaging carrier inhomogeneitties in ambipolar tellurene field effect transistors. *Nano Lett.* **19**, 1289–1284 (2019).
55. Dresselhaus, M. S., Dresselhaus, G., Saito, R. & Jorio, A. Raman spectroscopy of carbon nanotubes. *Phys. Rep.* **409**, 47–99 (2005).

Acknowledgements

P.D.Y. was supported by NSF/AFOSR under EFRI 2DARE grant no. EFMA-1433459, ARO grant no. W911NF-15-1-0574 and ASCENT, one of six centres in JUMP, a Semiconductor Research Corporation (SRC) programme sponsored by DARPA. P.D.Y. and W.W. were also supported by ARO grant no. W911NF-17-1-0573 and NSF under grant no. CMMI-1762698. J.J. and H.W. acknowledge support from the US Office of Naval Research for the TEM effort. S.G. and L.Y. are supported by National Science Foundation (NSF) CAREER grant no. DMR-1455346 and Air Force Office of Scientific Research (AFOSR) grant no. FA9550-17-1-0304. M.J.K. was supported in part by the Global Research and Development Center Program (2018K1A4A3A01064272) and Brain Pool Program (2019H1D3A2A01061938) through the National Research Foundation of Korea (NRF) funded by the Ministry of Science and ICT. Computational resources were provided by the Stampede of Teragrid at the Texas Advanced Computing Center (TACC) through XSEDE.

Author contributions

P.D.Y. and J.-K.Q. conceived the idea and proposed the Te-CNT and Te-BNNT research. J.-K.Q. and P.-Y.L. performed growth experiments and analysed experimental data. J.-K.Q., P.-Y.L., M.S., G.Q. and A.C. performed device fabrication and analysed the experimental data. S.-Q.Z. and Y.K.Y. prepared the BNNT samples. Y.W. and W.W. synthesized bare Te nanowires. S.H. and X.X. conducted and supervised the Raman measurements. J.J., Q.W., M.J.K. and H.-Y.W. performed and analysed the STEM measurements. S.G. and L.Y. performed and supervised the DFT calculations. J.-K.Q., P.-Y.L. and P.D.Y. co-wrote the manuscript.

Competing interests

The authors declare no competing interests.

Additional information

Supplementary information is available for this paper at https://doi.org/10.1038/s41928-020-0365-4.

Correspondence and requests for materials should be addressed to P.D.Y.

Reprints and permissions information is available at www.nature.com/reprints.

Publisher's note Springer Nature remains neutral with regard to jurisdictional claims in published maps and institutional affiliations.